Realization of an autonomous virtual acoustic black hole with piezoelectric patches

Samuel Quaegebeur, Ghislain Raze, Li Cheng, Gaëtan Kerschen

Realization of an autonomous virtual acoustic black hole with piezoelectric patches

Samuel Quaegebeur[a,*], Ghislain Raze[b], Li Cheng[c], Gaëtan Kerschen[b]

[a]*Univ Lyon, Ecole Centrale de Lyon, CNRS, ENTPE, LTDS, UMR5513, 69130 Ecully, France*
[b]*Department of Aerospace and Mechanical Engineering, University of Liège, Allée de la Découverte 9 B-4000 Liège, Belgium*
[c]*Department of Mechanical Engineering, The Hong Kong Polytechnic University, Hung Hom Kowloon, Hong Kong SAR, P. R. China*

Abstract

Acoustic black holes (ABHs) offer new opportunities for designing mechanical devices that can trap and reduce the vibrational energy of a system. Two long-lasting challenges of mechanical ABHs are their manufacturing and inability to operate at low frequencies. The recently-developed concept of a *virtual ABH* frees classical ABHs from these difficulties. Specifically, thanks to the digital implementation of the ABH impendance, any length, material or damping can in principle be realized, which opens the way to vibration mitigation at very low excitation frequencies. The concept was successfully implemented experimentally with an electrodynamic shaker in one of our previous publications. Obviously, the use of the shaker made the system bulky and non-autonomous. In this paper, piezoelectric patches are employed to realize the virtual ABH to form a self-contained and autonomous system which could thus find applications in real-life structures. However, piezoelectric VABHs raise theoretical and experimental difficulties which are discussed herein. An improved pseudo-collocated approach is developed, and the synthetic impedance is theoretically derived. Experiments are conducted using a cantilever beam where the virtual ABH is implemented with few piezoelectric patches. It is shown to provide excellent vibration reduction over a large frequency range, even at low excitation frequencies.

Keywords: Acoustic black hole, Piezoelectric, Vibration mitigation, Dynamic substructuring

1. Introduction

Reducing structural vibration remains one important topic of research in the mechanical community. A classical approach to mitigate the resonant vibrations of a structure (also called host structure) is the concept

*Corresponding author
Email address: samuel.quaegebeur@ec-lyon.fr (Samuel Quaegebeur)

of a tuned mass damper (TMD) developed in 1909 and realized using a spring-mass system [1]. In [2], a damper was added to the TMD. The augmented system exhibits two resonance peaks featuring a much lower amplitude than that of the uncontrolled structure. Despite its simplicity and effectiveness, the TMD can only attenuate the vibrations of a single resonance. Moreover, its tuning requires great care.

In 1988, Mironov proposed the concept of an acoustic black hole (ABH) [3] for vibration mitigation. The ABH corresponds to a tapered wedge beam whose thickness follows a power law profile. When used as a vibration mitigation device, it is attached to a host structure, and the vibrational energy of the coupled system gets localized inside the ABH device. To enhance the vibration reduction effects, damping layers were added to the ABH [4]. Unlike the TMD, the ABH can be effective in a wide frequency range and is not very sensitive to changes in the host structure. However, to be effective at low excitation frequency, the ABH must be very long [5, 6], which currently represents the main bottleneck of this concept. Moreover, due to the power law profile of the thickness, the ABH tip can be very thin and, hence, brittle and fragile. Typically, to achieve vibration reduction below 10 Hz with steel material, the tip might have a thickness around one hundred nanometers, which raises important manufacturing issues. Research has attempted to address this issue, see, e.g., [7, 8], but it still remains an open and unsolved question.

In this context, piezoelectric systems represent an interesting alternative to mechanical systems. A piezoelectric transducer converts mechanical energy into electrical energy. By connecting a shunt circuit (resistors and/or inductors in series or in parallel) to the transducer, energy dissipation can be achieved. The concept of a resonant piezoelectric shunt was first proposed by Hagood and Flotow [9] and was exploited in many applications since then [10, 11]. It was also used together with an ABH to enhance vibration mitigation [12, 13, 14]. One difficulty is that high inductances are required to tackle low-frequency modes. To remedy this problem, Flemming et al. [15] proposed the idea of a synthetic impedance where the electrodes of the piezoelectric material are connected to an electronic circuit driven by a digital unit that can implement any control law. This offers numerous possibilities [16, 17, 18], including nonlinear vibration absorbers [19] and rainbow trapping devices [20].

The idea to reproduce digitally the properties of an ABH to trap the energy was proposed in [21] . The wave compression property was also mimicked in [22]. In these papers, a large number of piezoelectric devices were used to digitally and gradually modify the beam's Young modulus. In the same spirit, Soleimanian et al. [23] reproduced the variations in ABH thickness with successive capacitors, which led to a maximum of 11% power radiation reduction in numerical simulations. Recently, we proposed the concept of a *virtual acoustic black hole* (VABH) where the mechanical ABH impedance, derived with a state-space

approach [24], is simulated digitally. All ABH properties, namely the low reflection coefficient, the energy trapping, and vibration mitigation can be reproduced with a VABH. Due to its virtual nature, any ABH can, in principle, be implemented. For instance, we considered ABHs which could hardly be manufactured, e.g., a 2 m long ABH featuring a 150 nm thickness at the tip. The experimental demonstration of the VABH concept led to excellent performance, i.e., all modes between 0 and 500 Hz could be attenuated by at least 12 dB. However, a shaker was employed to implement the VABH effect. Obviously, this made the system bulky and non-autonomous.

The main thrust of this paper lies in the theoretical and experimental investigations of the so-called VABH [24] with piezoelectric patches and a digital unit to form a self-contained and autonomous system, as depicted in Figure 1. This research thus offers a very compact implementation of a highly versatile ABH. Specifically, it will be shown that the proposed design solves the bottleneck problem of mechanical ABHs by allowing vibration mitigation at very low excitation frequencies. The resulting electromechanical problem is described in Section 2 for an improved pseudo-collocated approach. Section 3 is dedicated to numerical simulations. Section 4 presents the experimental results obtained using a cantilever beam as a host structure. Excellent vibration reduction is obtained with a small number of piezoelectric patches. Finally, conclusions are drawn in Section 5.

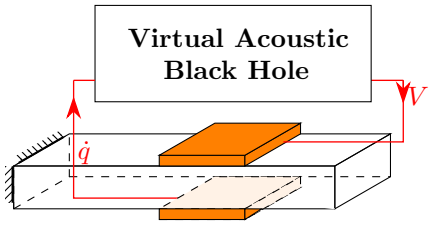

Figure 1: Schematics of the proposed implementation of the VABH.

2. Theoretical developments

2.1. VABH formulation

In this paper, the ABH effect is obtained by digital means. The ABH impedance is first derived. A uniform cantilever beam of length L, width b and thickness h_0 depicted in Figure 2 constitutes the host structure. The cantilever has traction-compression and flexural, but the focus is on the flexural modes. The beam is attached to an ABH comprising a tapered wedge beam of length $(L_{\mathrm{ABH}} - x_0)$ and width b, where x_0

denotes the residual truncation. The ABH thickness varies according to

$$h(x) = h_0 \left(\frac{L + L_{\mathrm{ABH}} - x}{L_{\mathrm{ABH}}} \right)^m, x \in [L, L + L_{\mathrm{ABH}} - x_0]. \tag{1}$$

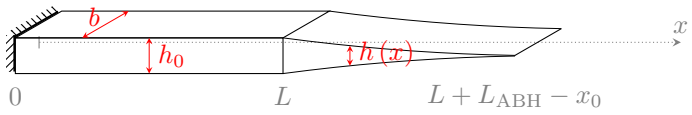

Figure 2: Cantilever beam with a mechanical ABH.

The readers are referred to [24] for a full description of the VABH formulation in state-space. In what follows, the ABH impedance is derived briefly using the Laplace transform.

The system is discretized using the finite element method. Each node is characterized by three displacements, namely the longitudinal (u), transversal (v), and rotational (ϕ) displacements. Superscripts b and tb denote the uniform and tapered wedge beams, respectively. For both systems, the internal and boundary nodes are represented by the subscripts I and B, respectively. The equations of motion read

$$\begin{bmatrix} \mathbf{M}^{\mathrm{b}}_{\mathrm{II}} & \mathbf{M}^{\mathrm{b}}_{\mathrm{IB}} \\ \mathbf{M}^{\mathrm{b}}_{\mathrm{BI}} & \mathbf{M}^{\mathrm{b}}_{\mathrm{BB}} \end{bmatrix} \begin{bmatrix} \ddot{\mathbf{x}}^{\mathrm{b}}_{\mathrm{I}} \\ \ddot{\mathbf{x}}_{\mathrm{B}} \end{bmatrix} + \begin{bmatrix} \mathbf{C}^{\mathrm{b}}_{\mathrm{II}} & \mathbf{C}^{\mathrm{b}}_{\mathrm{IB}} \\ \mathbf{C}^{\mathrm{b}}_{\mathrm{BI}} & \mathbf{C}^{\mathrm{b}}_{\mathrm{BB}} \end{bmatrix} \begin{bmatrix} \dot{\mathbf{x}}^{\mathrm{b}}_{\mathrm{I}} \\ \dot{\mathbf{x}}_{\mathrm{B}} \end{bmatrix} + \begin{bmatrix} \mathbf{K}^{\mathrm{b}}_{\mathrm{II}} & \mathbf{K}^{\mathrm{b}}_{\mathrm{IB}} \\ \mathbf{K}^{\mathrm{b}}_{\mathrm{BI}} & \mathbf{K}^{\mathrm{b}}_{\mathrm{BB}} \end{bmatrix} \begin{bmatrix} \mathbf{x}^{\mathrm{b}}_{\mathrm{I}} \\ \mathbf{x}_{\mathrm{B}} \end{bmatrix} = \begin{bmatrix} \mathbf{f}_{\mathrm{ext,I}} \\ \mathbf{f}_{\mathrm{ext,B}} + \mathbf{f}_{\mathrm{tb}\to\mathrm{b}} \end{bmatrix} \tag{2a}$$

$$\begin{bmatrix} \mathbf{M}^{\mathrm{tb}}_{\mathrm{II}} & \mathbf{M}^{\mathrm{tb}}_{\mathrm{IB}} \\ \mathbf{M}^{\mathrm{tb}}_{\mathrm{BI}} & \mathbf{M}^{\mathrm{tb}}_{\mathrm{BB}} \end{bmatrix} \begin{bmatrix} \ddot{\mathbf{x}}^{\mathrm{tb}}_{\mathrm{I}} \\ \ddot{\mathbf{x}}_{\mathrm{B}} \end{bmatrix} + \begin{bmatrix} \mathbf{C}^{\mathrm{tb}}_{\mathrm{II}} & \mathbf{C}^{\mathrm{tb}}_{\mathrm{IB}} \\ \mathbf{C}^{\mathrm{tb}}_{\mathrm{BI}} & \mathbf{C}^{\mathrm{tb}}_{\mathrm{BB}} \end{bmatrix} \begin{bmatrix} \dot{\mathbf{x}}^{\mathrm{tb}}_{\mathrm{I}} \\ \dot{\mathbf{x}}_{\mathrm{B}} \end{bmatrix} + \begin{bmatrix} \mathbf{K}^{\mathrm{tb}}_{\mathrm{II}} & \mathbf{K}^{\mathrm{tb}}_{\mathrm{IB}} \\ \mathbf{K}^{\mathrm{tb}}_{\mathrm{BI}} & \mathbf{K}^{\mathrm{tb}}_{\mathrm{BB}} \end{bmatrix} \begin{bmatrix} \mathbf{x}^{\mathrm{tb}}_{\mathrm{I}} \\ \mathbf{x}_{\mathrm{B}} \end{bmatrix} = \begin{bmatrix} \mathbf{0} \\ -\mathbf{f}_{\mathrm{tb}\to\mathrm{b}} \end{bmatrix}, \tag{2b}$$

where $\mathbf{M}$, $\mathbf{C}$, and $\mathbf{K}$ correspond to the mass, damping and stiffness matrices, respectively. External forces $\mathbf{f}_{\mathrm{ext}}$ are applied to the uniform beam. The internal forces, $\mathbf{f}_{\mathrm{tb}\to\mathrm{b}}$ are transmitted at the boundary between the two beams. Using the Laplace variable s, Equation (2b) becomes

$$\mathbf{X}^{\mathrm{tb}}_{\mathrm{I}} = \underbrace{-\left(s^2\mathbf{M}^{\mathrm{tb}}_{\mathrm{II}} + s\mathbf{C}^{\mathrm{tb}}_{\mathrm{II}} + \mathbf{K}^{\mathrm{tb}}_{\mathrm{II}}\right)^{-1}\left(s^2\mathbf{M}^{\mathrm{tb}}_{\mathrm{IB}} + s\mathbf{C}^{\mathrm{tb}}_{\mathrm{IB}} + \mathbf{K}^{\mathrm{tb}}_{\mathrm{IB}}\right)}_{\mathbf{Z}_{\mathrm{IB}}(s)} \mathbf{X}_{\mathrm{B}} \tag{3a}$$

$$-\mathbf{F}_{\mathrm{tb}\to\mathrm{b}} = \underbrace{\left[\left(s^2\mathbf{M}^{\mathrm{tb}}_{\mathrm{BI}} + s\mathbf{C}^{\mathrm{tb}}_{\mathrm{BI}} + \mathbf{K}^{\mathrm{tb}}_{\mathrm{BI}}\right)\mathbf{Z}_{\mathrm{IB}}(s) + \left(s^2\mathbf{M}^{\mathrm{tb}}_{\mathrm{BB}} + s\mathbf{C}^{\mathrm{tb}}_{\mathrm{BB}} + \mathbf{K}^{\mathrm{tb}}_{\mathrm{BB}}\right)\right]}_{\mathbf{Z}_{\mathrm{ABH}}(s)} \mathbf{X}_{\mathrm{B}} \tag{3b}$$

where $\mathbf{X}^{\mathrm{tb}}_{\mathrm{I}}$, $\mathbf{X}_{\mathrm{B}}$, and $\mathbf{F}_{\mathrm{tb}\to\mathrm{b}}$ are the Laplace transforms of $\mathbf{x}^{\mathrm{tb}}_{\mathrm{I}}$, $\mathbf{x}_{\mathrm{B}}$, and $\mathbf{f}_{\mathrm{tb}\to\mathrm{b}}$, respectively. The (3×3) $\mathbf{Z}_{\mathrm{ABH}}$ matrix is the ABH impedance.

2.2. *Mechanical system with piezoelectric patches*

In [24], the theory of Section 2.1 was implemented with an accelerometer and a shaker that applies the transversal component of $\mathbf{F}_{\text{tb}}$. This design allowed to demonstrate the feasibility of the VABH concept but it lacked compactness. The use of rectangular PZTs remedies this issue. When a PZT is deformed, a current is created between its electrodes. On the other hand, applying a voltage difference between its electrodes deforms the PZT, which applies forces and torques to the host structure.

The formulation proposed in this paper is referred to as pseudo-collocated. A beam composed of N pairs of identical collocated piezoelectric patches is considered, see Figure 3. The PZTs work together in pairs, see Figure 4. In one pair, one PZT is actuating the structure whereas the other is sensing its motion. This sensor is assumed to be connected to a perfect current sensing device and is thus considered to be in short circuit ($V_{i,\text{s}} = 0$).

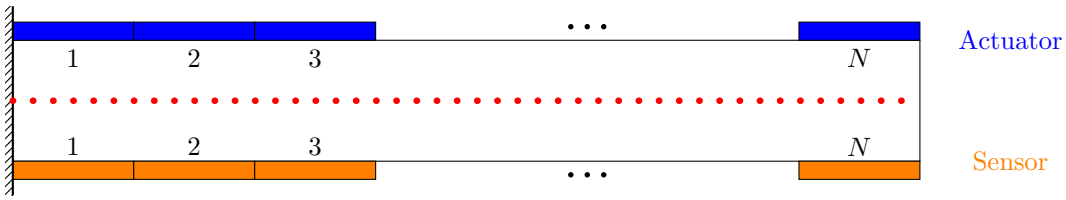

Figure 3: Beam covered with piezoelectric patches for the pseudo-collocated approach.

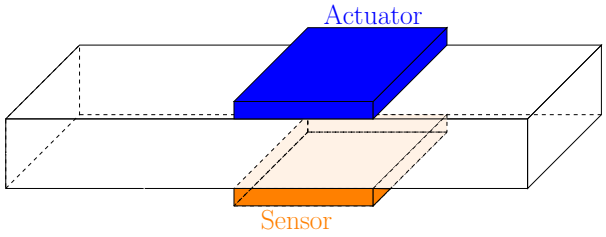

Figure 4: Classical pseudo-collocated approach.

The equations of motion of the system are

$$\begin{cases} \mathbf{M}\ddot{\mathbf{x}} + \mathbf{C}\dot{\mathbf{x}} + \mathbf{K}_{\text{sc}}\mathbf{x} + \displaystyle\sum_{i=1}^{N} (\boldsymbol{\Theta}_{i,\text{a}} C_p V_{i,\text{a}}) &= \mathbf{F} \\ \boldsymbol{\Theta}_{i,\text{a}}^{\mathsf{T}}\mathbf{x} - (C_p)^{-1} q_{i,\text{a}} = V_{i,\text{a}}, & \forall i \in [\![1,N]\!] \\ C_p \boldsymbol{\Theta}_{i,\text{s}}^{\mathsf{T}}\mathbf{x} = q_{i,\text{s}}, & \forall i \in [\![1,N]\!]. \end{cases} \tag{4}$$

The scalar C_p represents the capacitance at constant strain of a piezoelectric patch. The vector $\mathbf{x}$ $(3 \times N_{\text{nodes}})$ contains the displacements of all degrees of freedom

$$\mathbf{x} = \left[\underbrace{u_1, v_1, \phi_1}_{\text{node 1}}, \cdots, \underbrace{u_j, v_j, \phi_j}_{\text{node } j}, \cdots, \underbrace{u_k, v_k, \phi_k}_{\text{node } k}, \cdots, \underbrace{u_{N_{\text{nodes}}}, v_{N_{\text{nodes}}}, \phi_{N_{\text{nodes}}}}_{\text{node } N_{\text{nodes}}} \right]^{\mathsf{T}}, \tag{5}$$

where j and k are two arbitrary nodes. The matrices $\boldsymbol{\Theta}_{i,a}$ and $\boldsymbol{\Theta}_{i,s}$ are the ith PZT coupling vectors for the actuator and sensor, respectively [25]. Assuming that the boundaries of the ith PZT are connected to the nodes j and k and following the same layout as in Equation (5), these matrices read

$$\boldsymbol{\Theta}_{i,a} = \left[\underbrace{0,0,0}_{\text{node 1}}, \cdots, \underbrace{\theta_u, 0, -\theta_\phi}_{\text{node } j}, \cdots, \underbrace{-\theta_u, 0, \theta_\phi}_{\text{node } k}, \cdots, \underbrace{0,0,0}_{\text{node } N_{\text{nodes}}} \right]^{\mathsf{T}}. \tag{6}$$

$$\boldsymbol{\Theta}_{i,s} = \left[\underbrace{0,0,0}_{\text{node 1}}, \cdots, \underbrace{\theta_u, 0, \theta_\phi}_{\text{node } j}, \cdots, \underbrace{-\theta_u, 0, -\theta_\phi}_{\text{node } k}, \cdots, \underbrace{0,0,0}_{\text{node } N_{\text{nodes}}} \right]^{\mathsf{T}}. \tag{7}$$

where θ_u and θ_ϕ are two piezoelectric constants for the longitudinal and rotational displacements, respectively. Each constant is the same for all patches. The matrix $\mathbf{K}_{\text{sc}}$ is the stiffness matrix of the short-circuited system. The finite element method [25] is employed to compute all the quantities with the dynamics of the piezoelectric patches accounted for.

It is important to remark that, due to the simultaneous presence of both longitudinal and rotational effects, the coupling matrix can result in the instability of the pseudo-collocated approach, see [26, 27, 28] and references therein. The theoretical evidence for this is given in Appendix A. To remedy this issue, the design of the PZT connections proposed herein follows the idea in [27] and is represented in Figure 5. An actuator pair (or a sensor pair) is composed of two PZTs connected in parallel located at the lower and upper sides of the beam. The polarizations of the two PZTs are oriented in the same direction. As a result, the coupling matrix Θ_i is identical for both the actuator and sensor PZTs

$$\boldsymbol{\Theta}_{i,\text{a}} = \boldsymbol{\Theta}_{i,\text{s}} = \boldsymbol{\Theta}_i = \left[\underbrace{0,0,0}_{\text{node 1}}, \cdots, \underbrace{0,0,-2\theta_\phi}_{\text{node } j}, \cdots, \underbrace{0,0,2\theta_\phi}_{\text{node } k}, \cdots, \underbrace{0,0,0}_{\text{node } N_{\text{nodes}}} \right]^{\mathsf{T}}. \tag{8}$$

Moreover, the contributions of the longitudinal effects have now disappeared from the coupling matrix, removing the risk of a potential instability.

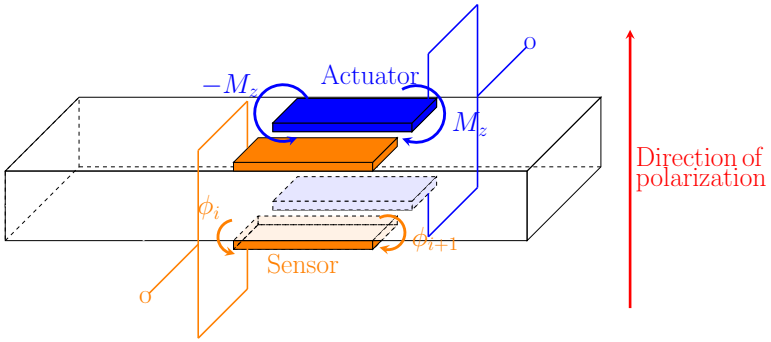

Figure 5: Improved layout for the PZTs.

The voltage applied $V_{i,\mathrm{a}}$ by a PZT is evaluated with the impedance Z_i implemented in the digital unit multiplied by the current sensed in the collocated PZT. In Laplace domain, this gives

$$V_{i,\mathrm{a}} \quad = \quad Z_i(s)Q_{i,\mathrm{s}} = Z_i(s)C_p\Theta_i^{\mathsf{T}}\mathbf{X} = 2Z_i(s)C_p\theta_\phi\Delta\phi_i, \tag{9}$$

The term $\Delta\phi_i$ represents the difference of rotation between the edges of the ith PZT. The notation $\left(\phi_i^{\mathrm{p}}\right)_{i\in[\![1,N]\!]}$ describes the rotation of the right edge of the ith PZT. The superscript p was introduced to distinguish between the rotation of an arbitrary node i and the rotation of a node connected to the edge of a PZT. Substituting (9) in the dynamics of the beam (4) and equating the result to the dynamics of the beam with ABH (2a), the equations

$$\begin{aligned} \left(2C_p\theta_\phi\right)^2 Z_N\Delta\phi_N &= -Z_{\mathrm{ABH},\phi}\phi_N^{\mathrm{p}} \\ \left(2C_p\theta_\phi\right)^2 Z_i\Delta\phi_i &= \left(2C_p\theta_\phi\right)^2 Z_{i+1}\Delta\phi_{i+1} \quad \forall i\in[\![1,N-1]\!]. \end{aligned} \tag{10}$$

must be satisfied. The first equation expresses the sought ABH effect: $Z_{\mathrm{ABH},\phi}$ denotes the torque component $Z_{3,3}$ of Z_{ABH} defined in Equation (3b). The second equation corresponds to the torques created by two adjacent patches which need to be cancelled out. The solution is

$$Z_i = \frac{-Z_{\mathrm{ABH},\phi}}{\left(2C_p\theta_\phi\right)^2}\left(\frac{\phi_N^{\mathrm{p}}}{\Delta\phi_i}\right) \quad \forall i\in[\![1,N]\!]. \tag{11}$$

Summing the measured charges (see the third equation in (4)) gives

$$\phi_N^{\mathrm{p}} = \frac{1}{\left(2C_p\theta_\phi\right)}\sum_{i=1}^{N} Q_{i,\mathrm{s}}. \tag{12}$$

Finally,

$$Z_i = \frac{-Z_{\mathrm{ABH},\phi}}{\left(2C_p\theta_\phi\right)^2 Q_{i,\mathrm{s}}}\sum_{i}^{N} Q_{i,\mathrm{s}} \quad \forall i\in[\![1,N]\!]. \tag{13}$$

and the voltage to be applied to each piezoelectric patch is equal to

$$V_{i,\mathrm{a}} \quad = \quad Z_i Q_{i,\mathrm{s}} = \frac{-Z_{\mathrm{ABH},\phi}}{\left(2C_p\theta_\phi\right)^2}\sum_i^N Q_{i,\mathrm{s}}. \tag{14}$$

Applying the ABH effect with this improved pseudo-collocated approach requires to sum the current of the sensing PZTs and to apply the same voltage at the electrodes of all actuating PZTs. A practical way to implement this is to connect all PZTs (sensing and actuating) in parallel. A single controller with $\frac{-Z_{\mathrm{ABH},\phi}}{\left(2C_p\theta_\phi\right)^2}$ is then defined.

3. Numerical results

The cantilever beam studied in [24] is considered herein. The beam is excited at its tip, and the transversal tip displacement is measured. Table 1 lists the beam parameters together with those of the mechanical ABH which will be implemented digitally through a VABH. The finite element method was employed for the discretization [29]. Both beam models were then reduced using a Craig-Bampton method [30] to decrease the computational cost. For the cantilever beam, 50 modes were retained to ensure excellent predictive accuracy between 0 and 500 Hz. 20 modes were kept for the ABH beam due to the limitation imposed by the real-time controller (RTC) processor. Beyond f_{off}, the highest eigenfrequency of the fixed modes kept in the Craig-Bampton reduction, the ABH dynamics is no longer described accurately. In addition, the ABH effect usually takes place above a cut-on frequency [5, 6] equal to

$$f_{\mathrm{on}} = \frac{h_0}{2\pi L_{ABH}^2}\sqrt{\frac{40E_{\mathrm{ABH}}}{12\rho_{ABH}}}. \tag{15}$$

According to Table 1, f_{on} is equal to 9 Hz. Therefore, the VABH effect is expected to occur in the frequency range $[f_{\mathrm{on}}, f_{\mathrm{off}}]$ represented by a colored rectangle along the $x-$axis in the next figures.

Parameter	Cantilever beam	Digital ABH	PZT
Length	$L = 1\,\mathrm{m}$	$L_{\mathrm{ABH}} = 1\,\mathrm{m}$	Variable
Width	$b = 20\,\mathrm{mm}$	$b = 20\,\mathrm{mm}$	$b_{\mathrm{p}} = 6.4\,\mathrm{mm}$
Thickness	$h_0 = 6\,\mathrm{mm}$	$m = 2, x_0 = 10\,\mathrm{mm}$	$h_{\mathrm{p}} = 0.23\,\mathrm{mm}$
Young modulus	$E_{\mathrm{b}} = 210\,\mathrm{GPa}$	$E_{\mathrm{ABH}} = 210\,\mathrm{GPa}$	$E_{\mathrm{p}} = 52\,\mathrm{GPa}$
Density	$\rho_{\mathrm{b}} = 7800\,\mathrm{kg\,m^{-3}}$	$\rho_{\mathrm{ABH}} = 7800\,\mathrm{kg\,m^{-3}}$	$\rho_{\mathrm{p}} = 7800\,\mathrm{kg\,m^{-3}}$
Modal damping	$\xi_{\mathrm{b}} = 0.05\%$	$\xi_{\mathrm{ABH}} = 5\%$	NA

Table 1: System parameters.

3.1. Improved pseudo-collocated approach

3.1.1. VABH performance

The cantilever beam is covered with ten PZT cells comprising each four PZTs as in Figure 5. They are placed next to each other, and their length is equal to 10 cm so that they cover the entire beam length [1]. The system's Bode plot in Figure 6 confirms that a perfect alternating pole-zero pattern is obtained; thus, a collocated system is achieved [28].

[1] Excellent vibration results can also be obtained when the PZTs are not placed exactly next to each other

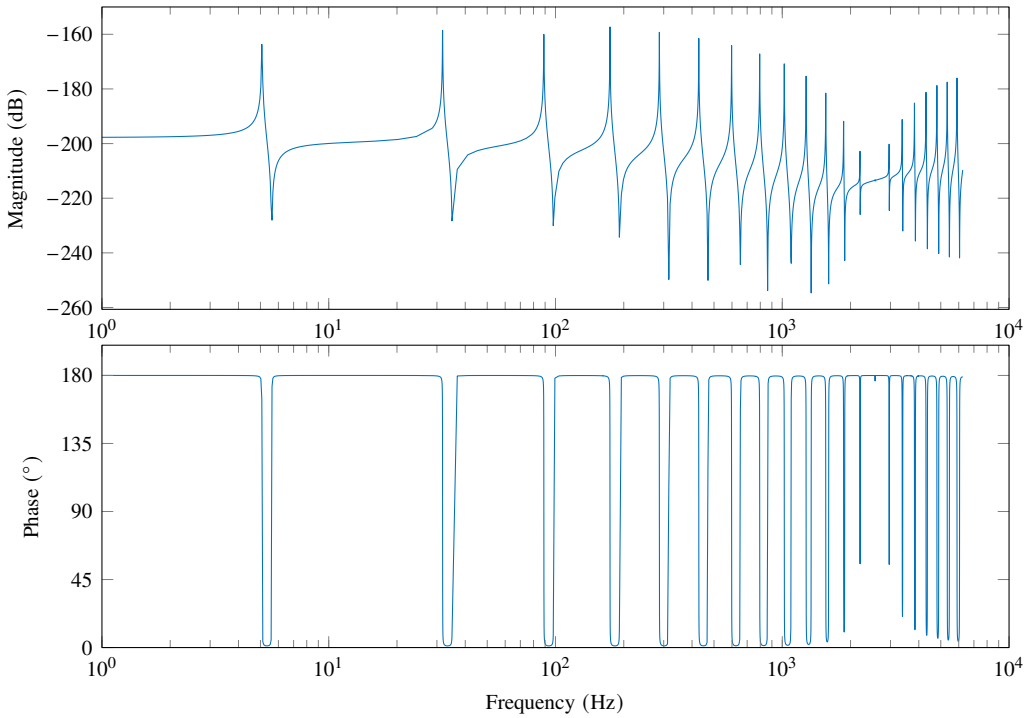

Figure 6: Bode plot of the improved pseudo-collocated approach.

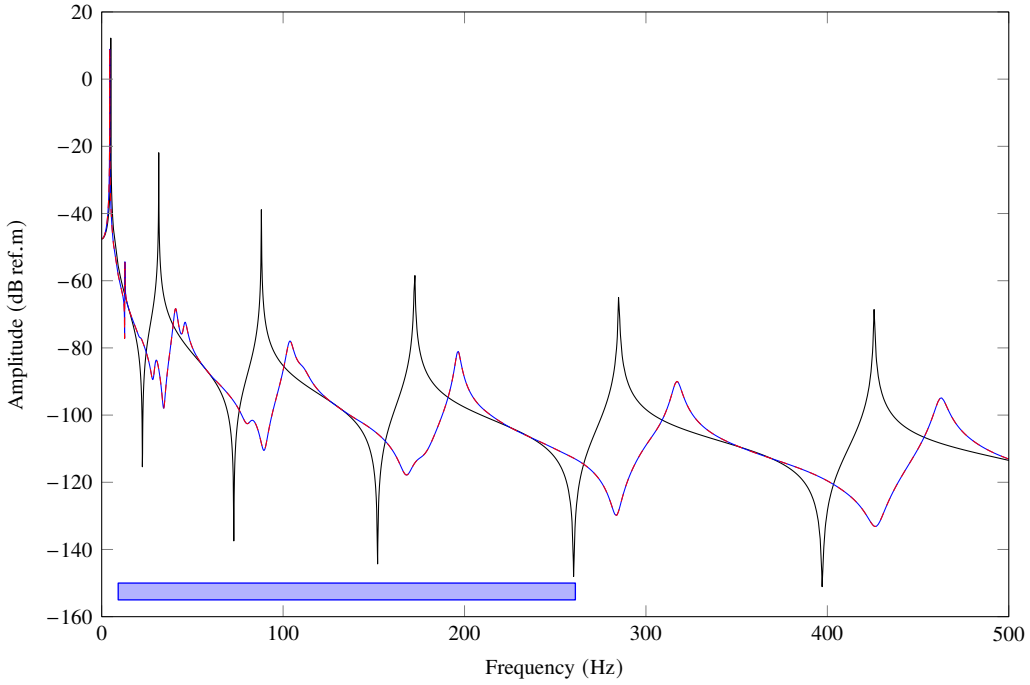

Figure 7: FRF of the pseudo-collocated approach with an ABH length of 1000 mm. (——): plant, (- -): reference VABH, and (- -): VABH with PZTs.

The frequency response function (FRF) obtained with the control law (14) is presented in Figure 7. The performance of the PZT-based VABH is seen to be identical to that of the reference VABH, i.e., the PZT-less ABH which applies directly the rotational component $Z_{\mathrm{ABH},\phi}$. They lead to excellent vibration mitigation (more than 20 dB of reduction) in the expected working range of the device. However, being below f_{on}, the amplitude of the first resonance peak cannot be attenuated. To address this limitation, the ABH length is increased up to 3000 mm in Figure 8. The VABH is now effective from 1 Hz and can then mitigate the vibrations around the first resonance. In this case, f_{off} is drastically reduced to 19.2 Hz due to the large number of VABH modes at low frequencies, as shown in Figure 8b.

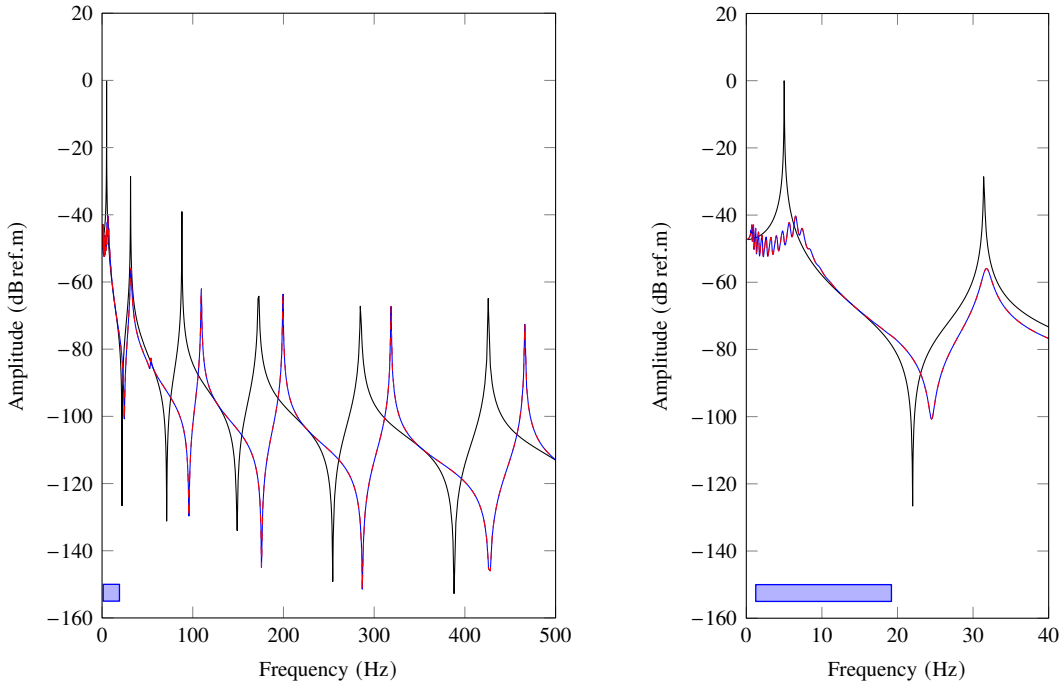

(a) Main response.

(b) Close-up.

Figure 8: FRF of the pseudo-collocated approach with an ABH length of 3000 mm. (——): plant, (- -): reference VABH, and (- -): VABH with PZTs.

Reference [8] showed that the ABH effect can also be reproduced if the ABH is not located at beam tip. To consider a more practical and compact implementation, a single cell comprising four PZTs of length 47.1 mm is placed at three different locations, namely near the clamping, in the middle of the beam and near the tip. The FRFs are displayed in Figure 9. The cell placed near the tip does not offer any reduction com-

pared to the plant since the strain there is very small. Conversely, the strain near the clamping is important for all modes; a cell placed at this location thus offers a performance comparable to that of the reference VABH. For the cell located in the middle of the beam, the VABH offers no reduction for modes 3 and 5 because the strain there is very small for these modes.

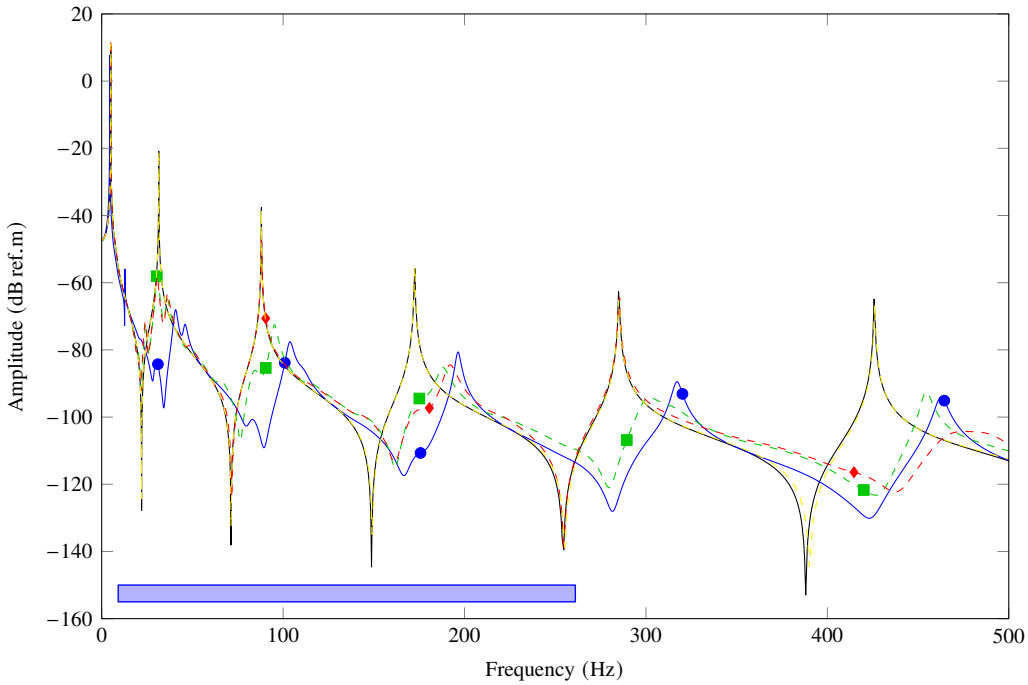

Figure 9: FRF of the pseudo-collocated approach with different PZT configurations. (—): plant, (—●—): reference VABH, (—■—): single cell at the clamping, (—♦—): single cell in the middle, (- - -): single cell at the tip.

Finally, the sensitivity with respect to the PZT parameter θ_ϕ is analyzed, because its value cannot be known very precisely experimentally. Figure 10 shows the FRFs with a single cell at the clamping for three different values of this parameter. When θ_ϕ is reduced by 50%, all peaks in the working range are still reduced by at least 20 dB. By decreasing the parameter much further, the reduction then only amounts to a few dB.

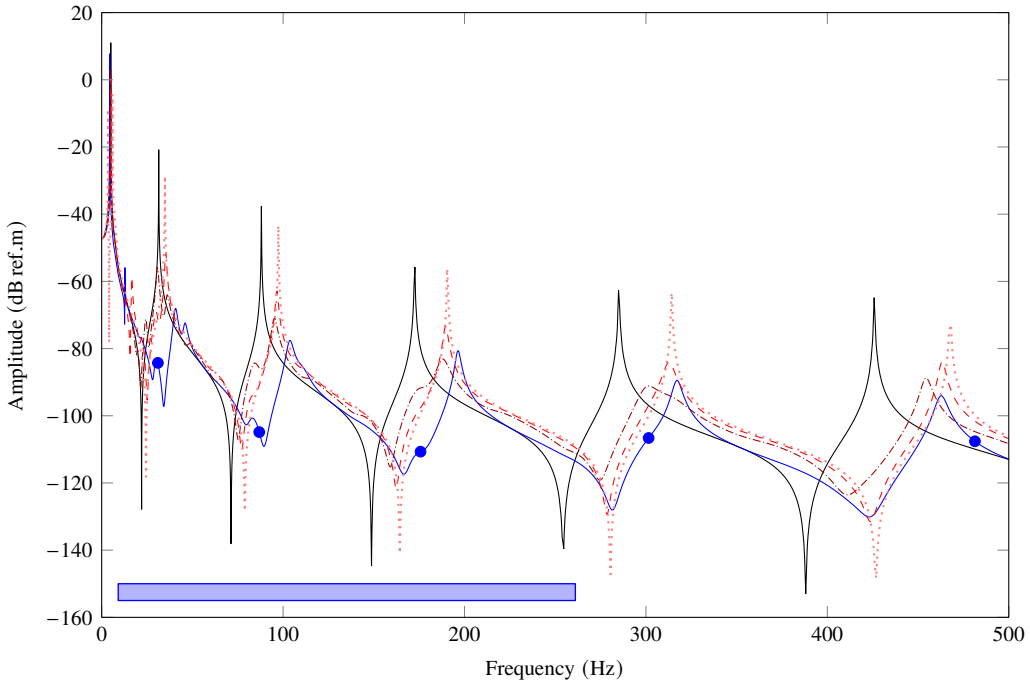

Figure 10: FRF of the pseudo-collocated approach for a single PZT cell near the clamping. (——): plant, (—●—): reference VABH, (-·-·-): VABH with PZTs (θ_ϕ), (- - -): VABH with PZTs ($0.5\theta_\phi$), (·····): VABH with PZTs ($0.1\theta_\phi$).

3.1.2. Energy dissipation brought by the VABH

This section provides physical insight into the VABH properties through the energy dissipated by structural damping and by the PZTs:

$$W_{\text{struct}} = \int_0^T \dot{\mathbf{x}}^\top \mathbf{C}\dot{\mathbf{x}}\mathrm{d}t, \quad W_{\text{PZT}} = \int_0^T \dot{\mathbf{x}}^\top \left(\sum_{i=1}^{N} \Theta_i C_p V_i\right) \mathrm{d}t. \tag{16}$$

These quantities are normalized by the energy brought by the external force $W_{\text{ext}} = \int_0^T \dot{\mathbf{x}}^\top \mathbf{f}_{\text{ext}}\mathrm{d}t$.

The cantilever beam is completely covered by 10 PZT cells. VABHs with different lengths and modal dampings are considered. Figure 11 illustrates the normalized energies when $L_{\text{ABH}} = 300\,\text{mm}$ and $\xi_{\text{ABH}} = 0.05\%$. At low excitation frequencies where the VABH is not effective, the dissipation is entirely due to structural damping. From 80 Hz, i.e., just below f_{on}, energy starts to be dissipated by the PZTs. However, due to the low modal damping, both the PZTs and structural damping dissipate a similar amount of vibrational energy. When $\xi_{\text{ABH}} = 5\%$ in Figure 12, the PZTs dissipate a much greater amount of energy. In fact, between 60 Hz and 500 Hz, more than 90% of the energy is dissipated by the PZTs except at the antiresonances. In

Figure 13, $L_{\text{ABH}} = 1000\,\text{mm}$ and $\xi_{\text{ABH}} = 5\%$, which corresponds to the case in Figure 7. The energy is
170 dissipated by the PZTs from as low as 6 Hz. Beyond f_{off}, the energy can still be dissipated by the PZTs, but the effect is lessened.

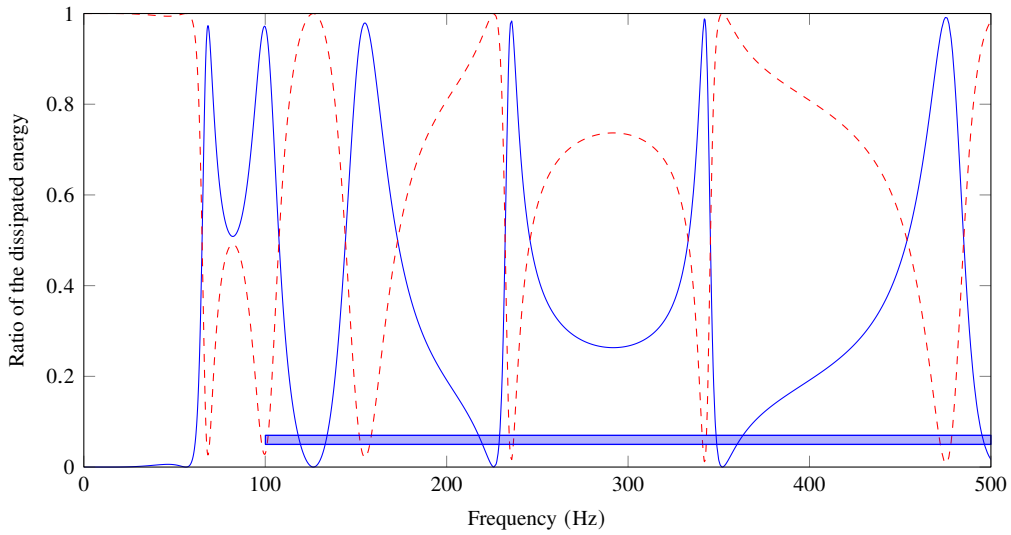

Figure 11: Energy dissipation for $\xi = 0.05\%$ and $L_{\text{ABH}} = 300\,\text{mm}$. (——): W_{PZT}, (- -): W_{struct}.

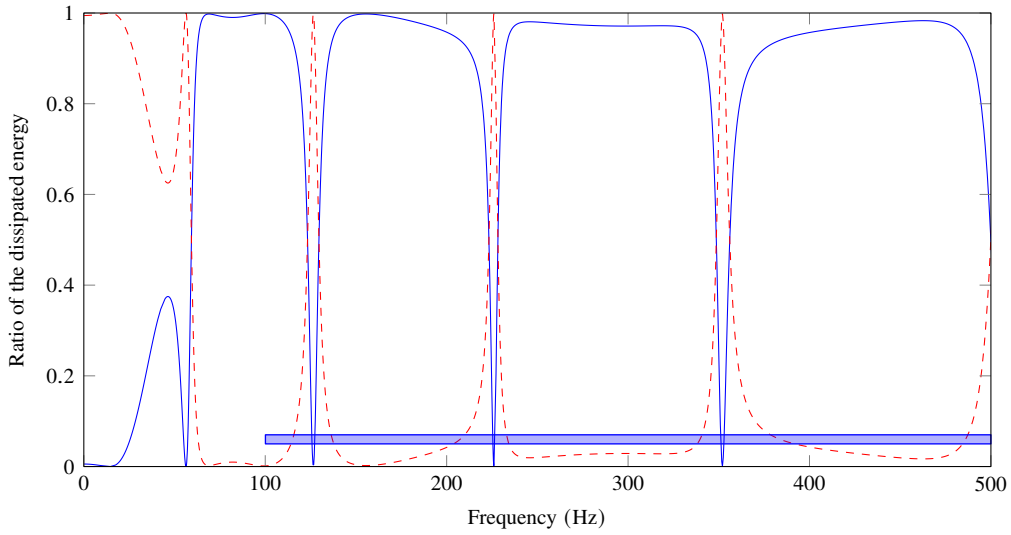

Figure 12: Energy dissipation for $\xi = 5\%$ and $L_{\text{ABH}} = 300\,\text{mm}$. (——): W_{PZT}, (- -): W_{struct}.

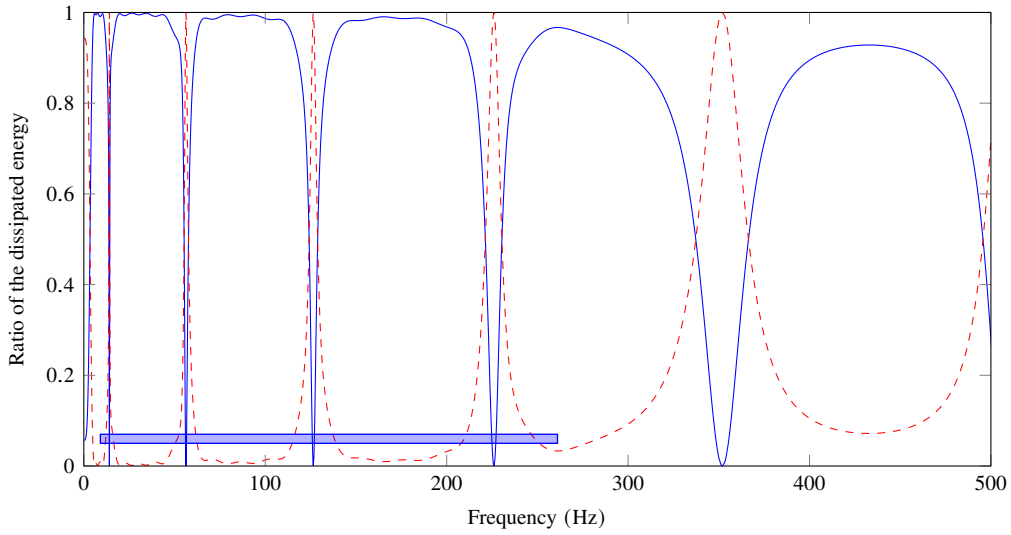

Figure 13: Energy dissipation for $\xi = 5\%$ and $L_{\text{ABH}} = 1000\,\text{mm}$. (——): W_{PZT}, (- -): W_{struct}.

3.2. A self-sensing approach

Another piezoelectric layout that could be envisioned for the VABH is a self-sensing approach for which the control law is imposed between the voltage and the current of a single PZT; this is portrayed in Figure 14. However, this approach results in an ill-conditioning of the control law and is thus not suitable for practical applications. The ill-conditioning is evidenced numerically with one pair of PZTs whose length is equal to the beam length. Following the theoretical derivations in Appendix B, the PZT impedance is

$$Z_1 = \frac{1}{C_p}\left(\frac{4C_p\theta_\phi^2}{4C_p\theta_\phi^2 + Z_{\text{ABH},\phi}} - 1\right). \tag{17}$$

Figure 15 shows that, if the VABH with the nominal value for C_p offers excellent vibration reduction, a 0.1% decrease in C_p yields a completely different FRF, which is almost coincident with that of the uncontrolled system.

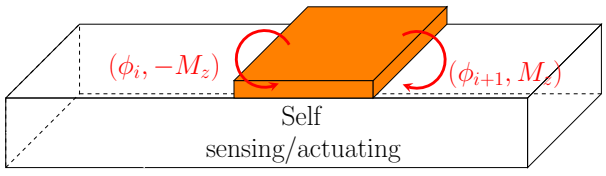

Figure 14: Self-sensing approach.

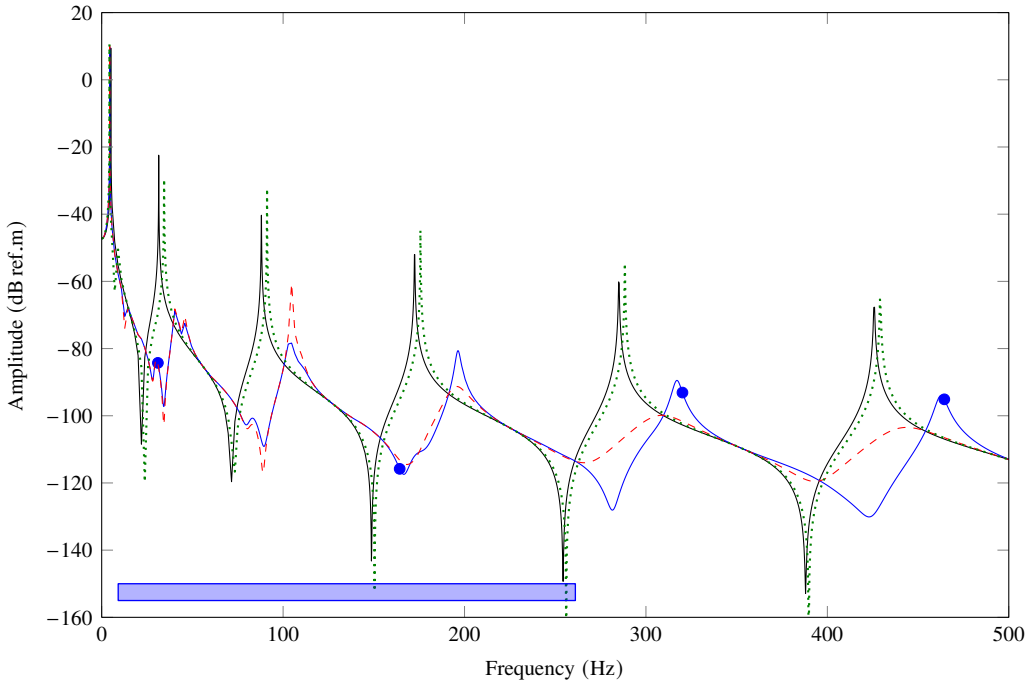

Figure 15: FRF of the self-sensing approach. (——): plant, (—●—): reference VABH, (- - -): VABH with PZTs, and (·····): VABH with PZTs with a 0.1% decrease of C_p.

4. Experimental demonstration

4.1. Experimental setup

Figure 16 presents the experimental cantilever beam whose parameters are listed in Table 1. The excitation signal was generated with an electrodynamic shaker connected to a real-time controller (RTC) dSPACE MicroLabBox and connected to the beam using a nylon stinger and an impedance head. The signal was a multi-sine function in the $[0.1\,\mathrm{Hz}, 1000\,\mathrm{Hz}]$ frequency interval with an amplitude of 0.01V. The gain between the command in volt and the applied force was $160\,\mathrm{N\,V^{-1}}$. The excitation was applied at 40% of the beam length from the clamped side. The sampling frequency was set to 40kHz.

Three cells of four PZTs (PSI-5A4E piezoceramic with $C_p = 28\,\mathrm{nF}$) were glued to the beam to realize the improved pseudo-collocated approach. The dimensions were: length=45.7 mm, width=6.4 mm and thickness=0.23 mm. The value of θ_ϕ was estimated to be $1.1 \times 10^4\,\mathrm{N\,C^{-1}}$. The gap between the first cell of PZTs and the clamping was 5 mm. The longitudinal gap between the PZTs was equal to 2 mm. Even if

several cells connected in parallel gave successful results, only the results with a single cell are discussed herein for conciseness. The main difference between this setup and the one in [24] is that the controller reproducing the ABH effect is implemented with PZTs. An autonomous and a very compact design is thus proposed.

Contrary to PZTs, the dSPACE MicroLabBox cannot handle large voltages; it is restricted to a range of amplitude of 10 V. To deal with appropriate voltages, analog electronics with operational amplifiers was employed. For the actuator, the analog circuit presented in Figure 17a consists of a voltage amplifier

$$V_a = \left(1 + \frac{R_2}{R_1}\right) V_{\text{DAC}}, \tag{18}$$

with R_i the resistors of the circuits and V_{DAC} the output voltage of dSPACE. A current amplifier and a low-pass filter were used after the sensing unit

$$V_{\text{ADC}} = \frac{R_s}{1 + \mathrm{i}\omega R_s C_s} \dot{q}_s, \tag{19}$$

where C_s is a capacitor, and V_{ADC} is the voltage at the input of dSPACE. The cut-off frequency of the low-pass filter was set to approximately 16 kHz to avoid noise pollution and aliasing of the signals. The values of the electronic components are listed in Table 2.

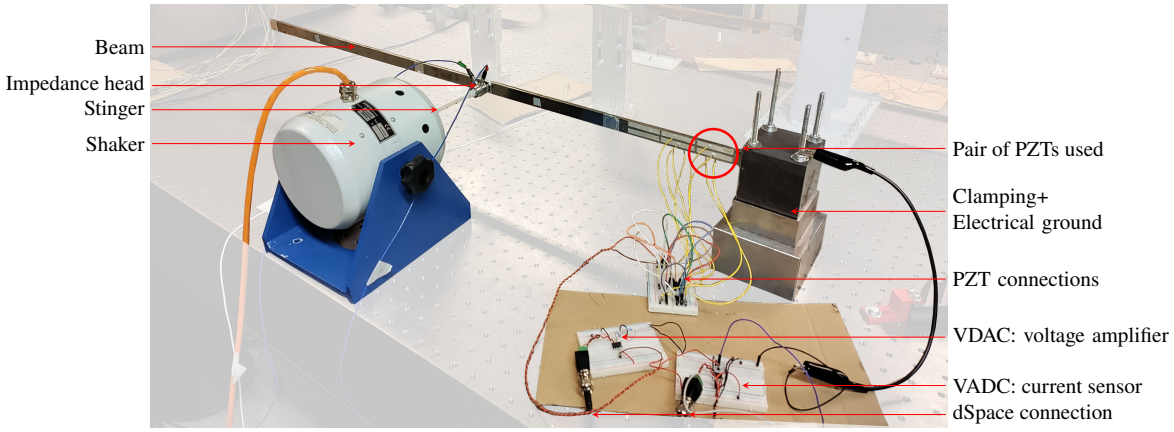

Figure 16: Experimental setup.

Parameters	R_1	R_2	R_s	C_s
Value	22 kΩ	10 kΩ	100 kΩ	0.1 nF

Table 2: Parameters of the electronic components.

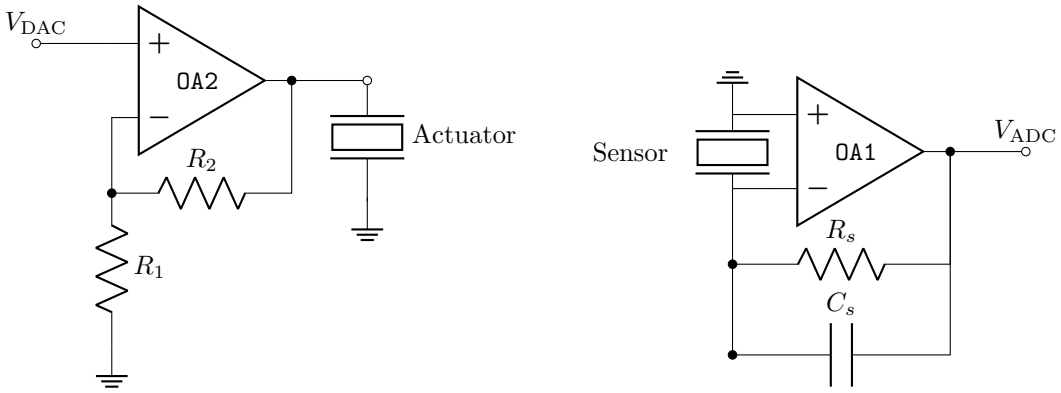

(a) VDAC: electrical circuit 1.

(b) VADC: electrical circuit 2.

Figure 17: Schematics of the analog circuits.

VABHs with different lengths were considered, see Table 3. The material was steel, and the truncation x_0 was set to 1 mm with a power law exponent equal to $m = 2$. The modal damping was set to 50%.

Because the first resonance of the experimental beam around 5 Hz has a very low magnitude, the focus is on the next six resonance peaks whose frequencies are given in Table 4.

Parameter	**VABH 1**	**VABH 2**	**VABH 3**	**VABH 4**
Length L_{ABH} (in mm)	1000	700	500	400

Table 3: Length of the different VABHs.

Peak 1	**Peak 2**	**Peak 3**	**Peak 4**	**Peak 5**	**Peak 6**
31.5 Hz	89.5 Hz	176 Hz	283.5 Hz	595 Hz	816.5 Hz

Table 4: Resonance frequencies of the plant.

4.2. Open-loop features

The plant transfer function for a single PZT cell is $\frac{\dot{q}_s}{V_a}$. All VABH transfer functions have two more zeros than poles and are thus improper. An additional pole acting as an integrator to obtain the charge from the sensed current was added to the function Z_{ABH} at $s = 0$ (see Equation 14). As it has still one more zero than poles, the resulting VABH remains improper. As an example, VABH 1 was numerically implemented. The

Bode plot is depicted in Figure 18. Initially, the magnitude increases by approximately 20 dB/decade due to the additional zero of the system. Due to the analog circuit and the first-order low-pass filter, the magnitude becomes relatively constant at high frequencies.

To make a digital implementation possible, the VABH transfer function must be proper. Furthermore, the closed-loop system is neutrally stable if the open-loop transfer function is equal to -1. A sufficient condition to guarantee stability in our setting is that the magnitude of the open-loop transfer function be smaller than 0 dB when the phase crosses -180° [31]. Notice that the conversion from analog to digital data (and inversely) leads to additional delays in the system and thus an additional phase lag. Therefore, in practice, having a magnitude greater than 0 dB when the phase is close to -180° is likely to result in an unstable closed-loop system. The black circles in Figure 18 highlight problematic frequency regions. Around 670 Hz, it is believed that the open-loop system has a phase close to -180° due to noise. Because the gain margin is close to 10 dB, no instabilities should rise from this area. Conversely, the circles around 8250 Hz and 9120 Hz correspond to magnitudes greater than 0 dB.

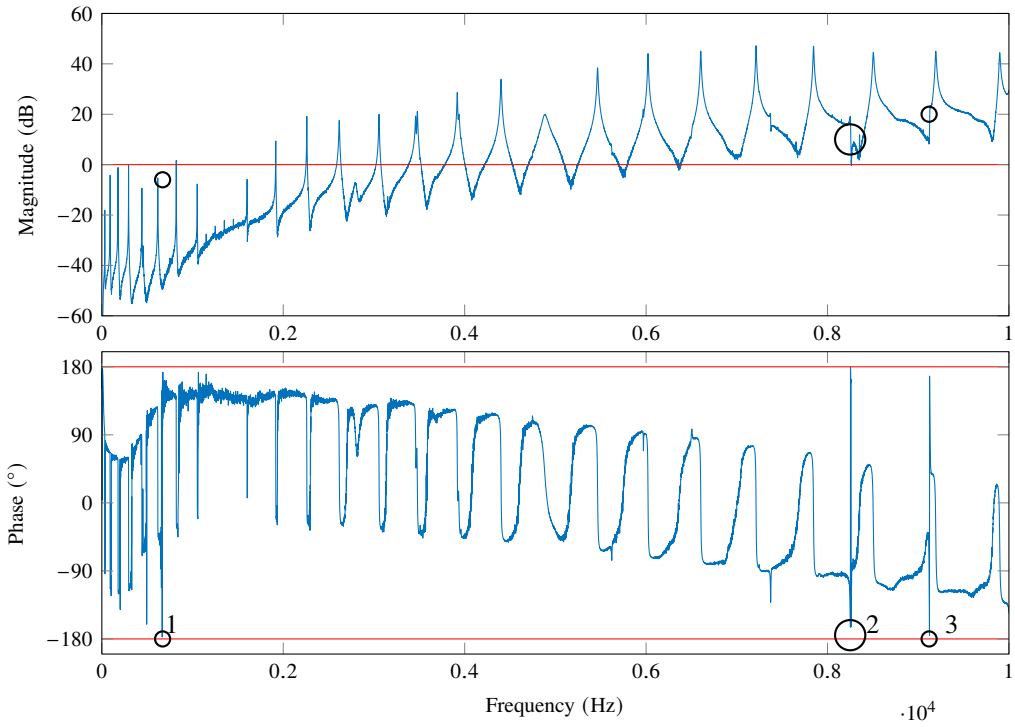

Figure 18: Bode plot of the open-loop transfer function for one PZT cell. Black circles denote potential instabilities.

Both issues (proper feature of the controller and stability of the closed-loop system) were solved by adding second-order low-pass filters to the controller:

$$h = \frac{\omega_{\mathrm{LP}}^2}{s^2 + s\omega_{\mathrm{LP}} + \omega_{\mathrm{LP}}^2}. \tag{20}$$

where ω_{LP} is the cut-off frequency. Using these filters was not straightforward. Although the magnitude of the open-loop system is lowered, its phase is also decreased. The potential areas of instabilities are thus shifted to lower frequencies where the magnitude may still be greater than 0 dB. Moreover, setting a too low value of ω_{LP} restricts the working range of the VABH. In what follows, two filters multiplied the VABH control law with $\omega_{\mathrm{LP},1} = 2\pi \times 1000\mathrm{rad/s}$ and $\omega_{\mathrm{LP},2} = 2\pi \times 1100\mathrm{rad/s}$. The experimental FRFs are represented in the range $[20\,\mathrm{Hz}, 1000\,\mathrm{Hz}]$ where the low-pass filters should not influence the results.

4.3. VABH performance

The FRFs of VABHs 2-4 are depicted in Figure 19, and their respective performance is summarized in Table 5. Excellent vibration reduction is obtained for the first five peaks with a length of 700 mm. Peak 6 is beyond the working range of this VABH and is thus not attenuated. When $L_{\mathrm{ABH}} = 400\,\mathrm{mm}$, the first peak is below the cut-on frequency of the VABH. However, peak 6, which lies in the working range of the VABH, is amplified. A similar amplification is also obtained when $L_{\mathrm{ABH}} = 500\,\mathrm{mm}$. This phenomenon may come from a coupling between the cut-off frequency of the low-pass filter and the one from the Craig-Bampton reduction. Nevertheless, for these two VABHs, greater vibration attenuation is achieved for peaks 2-4.

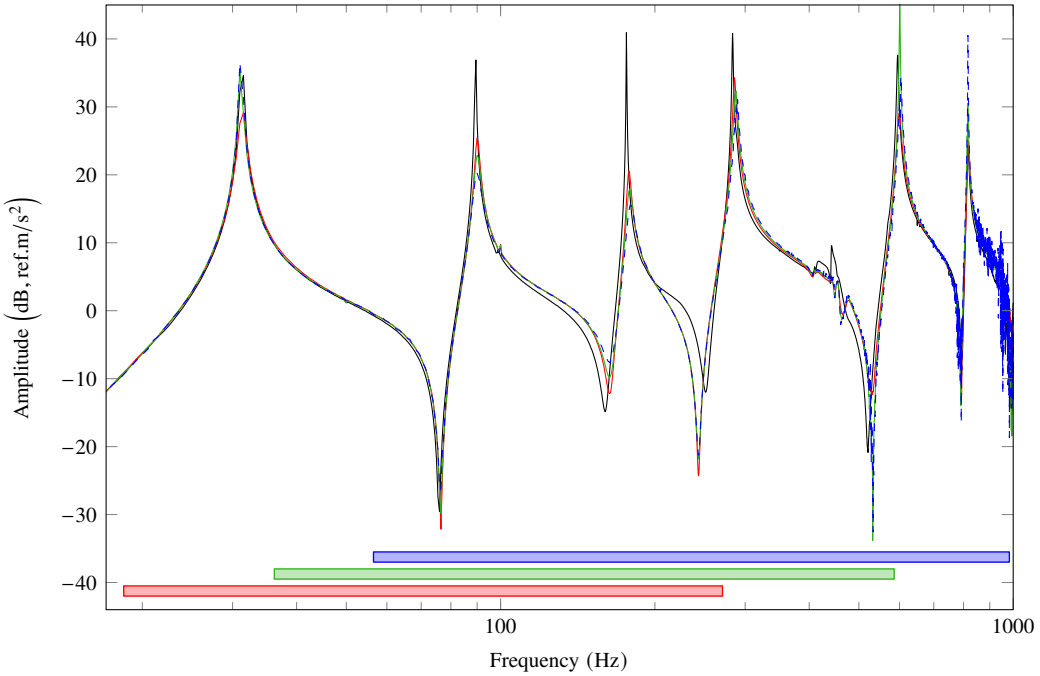

Figure 19: FRF with one PZT cell (accelerance at the shaker location). (—): plant, (—): $L_{\text{ABH}} = 700\,\text{mm}$, (—): $L_{\text{ABH}} = 500\,\text{mm}$, and (—): $L_{\text{ABH}} = 400\,\text{mm}$.

Type VABH	**Peak 1**	**Peak 2**	**Peak 3**	**Peak 4**	**Peak 5**	**Peak 6**
$L_{\text{ABH}} = 400\,\text{mm}$	-2	17	25	10	3	-16
$L_{\text{ABH}} = 500\,\text{mm}$	0	14	23	9	-9	-6
$L_{\text{ABH}} = 700\,\text{mm}$	4	12	20	7	8	0

Table 5: Vibration attenuation in dB.

The impact of the controller gain is now studied for VABH 3. Physically, increasing the gain is equivalent to considering a VABH whose mass, stiffness and damping matrices have been multiplied by this gain. Overall, Figure 20 and Table 6 confirm that increasing the gain allows for better vibration reduction. This comes, however, at the expense of reduced gain margins. At high frequencies, the FRF for the greatest gain becomes quite noisy; increasing the gain further would have resulted in an unstable closed-loop system.

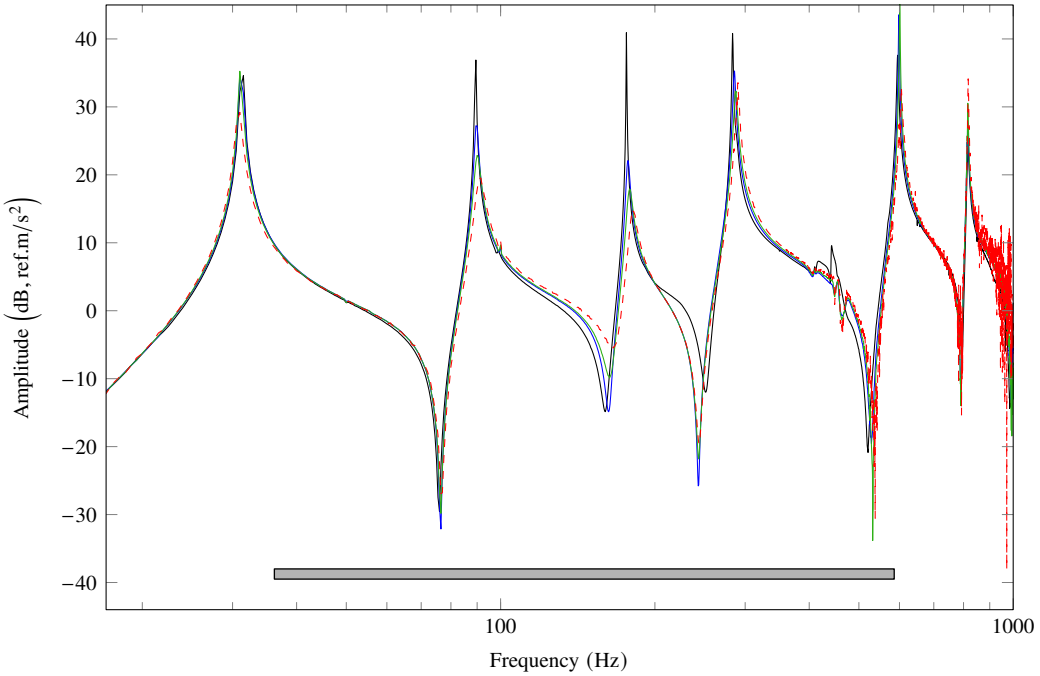

Figure 20: FRF for VABH 3 with different gain values. (—): plant, (—): gain of 2, (—): gain of 1, and (—): gain of 0.5.

Gain	Peak 1	Peak 2	Peak 3	Peak 4	Peak 5	Peak 6
0.5	0	7	19	6	-5	-3
1	0	14	23	9	-9	-6
2	5	27	26	8	5	-10

Table 6: Vibration attenuation in dB for VABH3 with different gains.

To optimize VABH performance, specific low-pass filters are now designed for each considered VABH. Indeed, by adapting ω_{LP}, the stability margins can be increased, enabling the gain to be increased. VABHs with lengths equal to 1000 mm, 700 mm and 500 mm are considered. Their gain is set to 1, 1.5, and 2, respectively. The FRFs are displayed in Figure 21 and the corresponding peak attenuations are listed in Table 7. In all cases, all peaks are reduced by at least 3 dB. The VABH with the highest gain and $L_{\text{ABH}} =$ 500 mm provides overall the best attenuation.

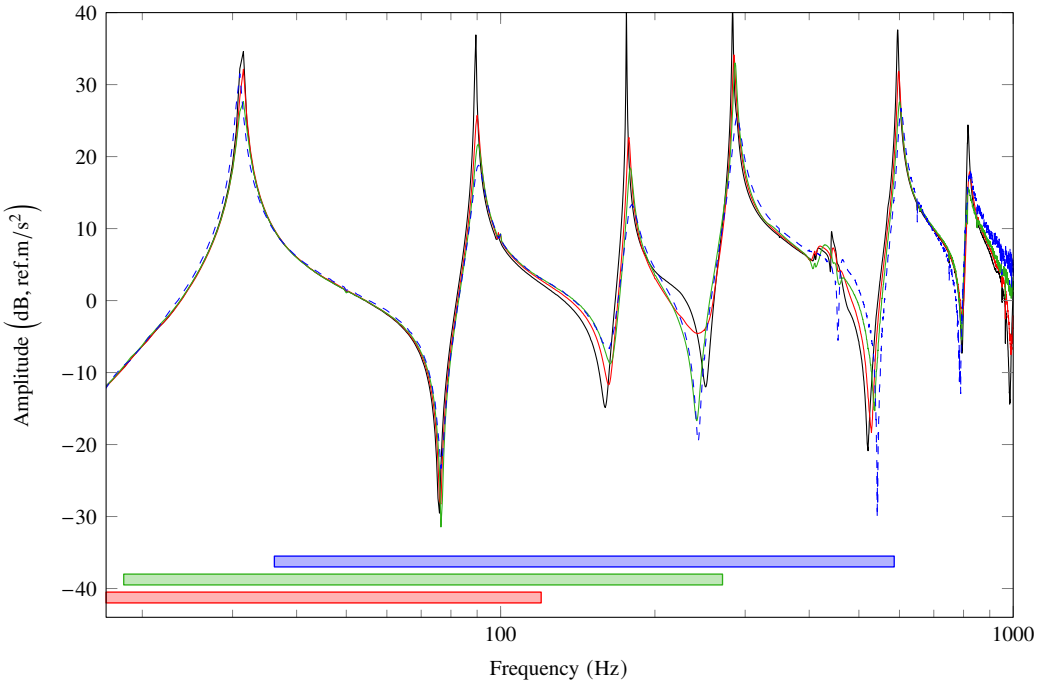

Figure 21: FRF with low-pass filter tuning. (—): plant, (—): $L_{\mathrm{ABH}} = 1000\,\mathrm{mm}$, (—): $L_{\mathrm{ABH}} = 700\,\mathrm{mm}$, and (—): $L_{\mathrm{ABH}} = 500\,\mathrm{mm}$.

Type VABH	Peak 1	Peak 2	Peak 3	Peak 4	Peak 5	Peak 6
$L_{\mathrm{ABH}} = 500\,\mathrm{mm}$	3	18	28	15	12	6
$L_{\mathrm{ABH}} = 700\,\mathrm{mm}$	7	15	22	8	11	9
$L_{\mathrm{ABH}} = 1000\,\mathrm{mm}$	3	11	18	7	7	6

Table 7: Improved VABH performance with low-pass filter tuning.

5. Conclusion

Piezoelectric transducers and digital controllers are exploited in this paper to reproduce the rotational effect of a mechanical ABH, which, in turn, allows for the realization of a compact and autonomous virtual acoustic black hole (VABH). The piezoelectric layout follows an improved pseudo-collocated approach with cells made of four PZT patches. It was shown that excellent vibration attenuation can be obtained even with a single PZT cell located where the strain energy is important.

The proposed VABH concept was demonstrated numerically and experimentally using a cantilever beam and exhibited impressive performance. However, great care which includes the design of a low-pass filter is needed to guarantee the stability of the closed-loop system. The impact of different parameters including the VABH length, the controller gain and the cut-off frequency of the filter was carefully investigated.

The VABH remedies to all ABH classical difficulties, e.g., reduction at low excitation frequencies, manufacture and brittleness issues. Its potential is hindered only by these stability issues and by the processor of the real-time controller. In this study, the processor limited the number of modes to be retained during the Craig-Bampton process to 20. Eventually, this reduces the VABH performance at higher frequencies.

Two perspectives of this work could be (i) a more systematic design of the low pass filters in order to progress toward a "plug and play" VABH which would require very few a priori knowledge about the host structure and (ii) the application of the VABH to more complex structures including, e.g., plates or cyclic systems.

Acknowledgement

Samuel Quaegebeur is thankful for the financial support of the ANR (project ANR-22-CPJ2-0061-01). This work was also supported by the Fonds de la Recherche Scientifique - FNRS under Grant n° [FRS-FNRS PDR T.0124.21], which is gratefully acknowledged. Li Cheng also thanks the support from the Research Grant Council of the Hong Kong SAR (PolyU 152023/20E).

Appendix

A. Noncollocated nature of the pseudo-collocated PZT configuration

A.1. Theoretical developments

This section provides mathematical insights into the noncollocated nature of the system in Figure 4. For simplicity, Equation (4) is written without damping and external forcing, and a single PZT cell is used:

$$\begin{cases} \mathbf{M}\ddot{\mathbf{x}} + \mathbf{K}_{\text{sc}}\mathbf{x} + \boldsymbol{\Theta}_a C_p V_{\text{a}} = \mathbf{0} \\ C_p \boldsymbol{\Theta}_s^{\intercal}\mathbf{x} = q_{\text{s}}. \end{cases} \tag{21}$$

To derive the plant transfer function q_s/V_a, the eigenvalue problem of the short-circuit system is solved. ω_n and $\boldsymbol{\alpha}_n$ represent the eigenfrequency and the normalized mode shape of mode n, respectively:

$$\mathbf{x} = \boldsymbol{\alpha}\boldsymbol{\eta} \qquad \boldsymbol{\alpha}^{\intercal}\mathbf{M}\boldsymbol{\alpha} = \mathbf{I} \qquad \boldsymbol{\alpha}^{\intercal}\mathbf{K}\boldsymbol{\alpha} = \boldsymbol{\Omega}^2, \tag{22}$$

where $\boldsymbol{\eta}$ is the vector of generalized control coordinates, $\mathbf{I}$ is the identity matrix and $\boldsymbol{\Omega}$ is a diagonal matrix comprising the eigenfrequencies. Substituting $\mathbf{x}$ by $\boldsymbol{\alpha}\boldsymbol{\eta}$ in (21), projecting the equations along $\boldsymbol{\alpha}$ and using (22) yields

$$\begin{cases} \left(-\omega^2\mathbf{I}+\boldsymbol{\Omega}^2\right)\boldsymbol{\eta}+\boldsymbol{\alpha}^\intercal\boldsymbol{\Theta}_a C_p V_\mathrm{a}=\mathbf{0} \\ C_p\boldsymbol{\Theta}_s^\intercal\boldsymbol{\alpha}\boldsymbol{\eta}=q_\mathrm{s}, \end{cases} \tag{23}$$

where ω is the excitation frequency. Considering expressions (6) and (7), the following relations are obtained:

$$\boldsymbol{\Theta}_s^\intercal\boldsymbol{\alpha}=\theta_u\boldsymbol{\alpha}_u+\theta_\phi\boldsymbol{\alpha}_\phi \tag{24a}$$

$$\boldsymbol{\alpha}^\intercal\boldsymbol{\Theta}_a=\theta_u\boldsymbol{\alpha}_u-\theta_\phi\boldsymbol{\alpha}_\phi, \tag{24b}$$

where $\boldsymbol{\alpha}_u$ and $\boldsymbol{\alpha}_\phi$ represent the projected modes $\boldsymbol{\alpha}$ on the coupling matrix $\boldsymbol{\Theta}$ when only the u and ϕ components are retained, respectively. Substituting these relations in (23) and expressing $\boldsymbol{\eta}$ as a function of V_a gives

$$\frac{q_s}{V_a}=-C_p^2\sum_{n=1}^{3N_\mathrm{nodes}}\left(\frac{\left(\theta_u\alpha_{u,n}+\theta_\phi\alpha_{\phi,n}\right)\left(\theta_u\alpha_{u,n}-\theta_\phi\alpha_{\phi,n}\right)}{-\omega^2+\omega_n^2}\right), \tag{25}$$

which after expansion finally yields

$$\frac{q_s}{V_a}=-C_p^2\sum_{n=1}^{3N_\mathrm{nodes}}\left(\frac{\left(\theta_u\alpha_{u,n}\right)^2}{-\omega^2+\omega_n^2}-\frac{\left(\theta_\phi\alpha_{\phi,n}\right)^2}{-\omega^2+\omega_n^2}\right). \tag{26}$$

Due to the different signs for the terms in $\alpha_{u,n}$ and $\alpha_{\phi,n}$, the transfer function q_s/V_a is not monotonous. As a consequence, the alternating poles/zeros pattern is not achieved, which may result in an unstable closed-loop system [28].

A.2. Numerical results

The sensing PZTs are connected in parallel to retrieve the sum of the currents (and hence the displacement at beam tip). Similarly, the actuating PZTs are also connected in parallel to apply the same voltage and to obtain a single resulting moment at beam tip. The current over voltage Bode plot of the system is depicted in Figure 22. If the system were collocated, the poles and zeros should alternate with the result that the phase should be comprised within a 180°-wide interval. However, this feature is lost around 1300 Hz where a traction-compression mode exists, which leads to a noncollocated system. To move away from an unstable closed-loop system, a low-pass filter with a cut-off frequency well below the traction-compression mode could be considered within the controller with the drawback that this would reduce the frequency range in

which the VABH is effective. The improved pseudo-collocated PZT layout proposed in Figure 5 represents a better solution to this issue.

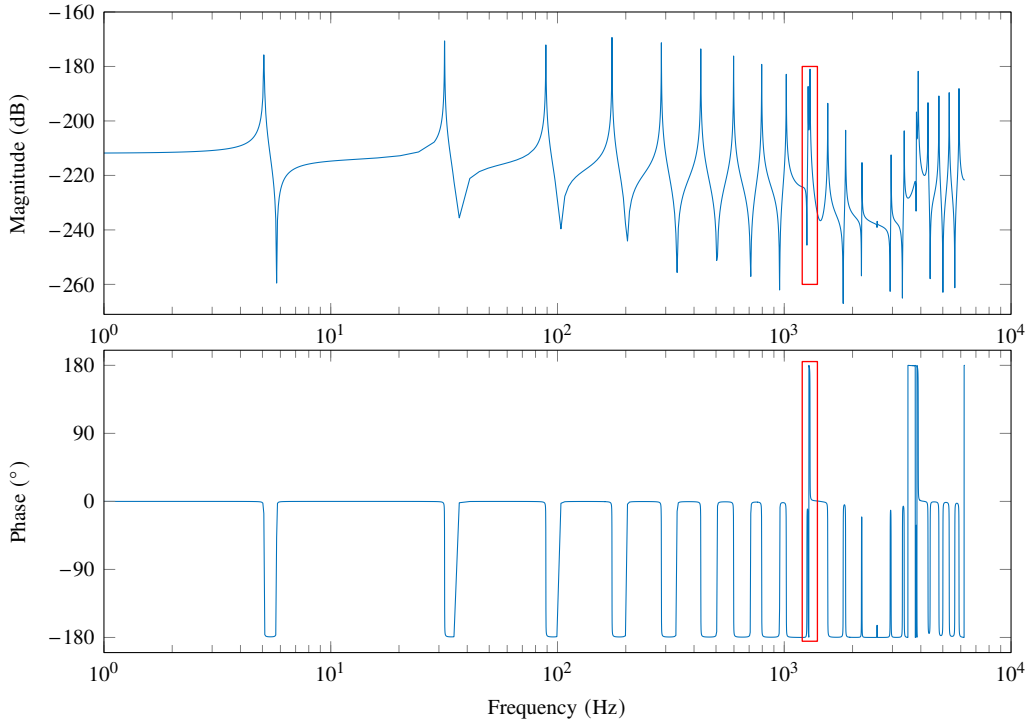

Figure 22: Bode plot of the pseudo-collocated PZT configuration. The red rectangle highlights the first traction-compression mode.

B. *Derivation of the impedance for the self-sensing approach*

The equations of motion of the system are

$$\begin{cases} \mathbf{M}\ddot{\mathbf{x}} + \mathbf{C}\dot{\mathbf{x}} + \mathbf{K}_{\text{sc}}\mathbf{x} + \sum_{i=1}^{N} (\boldsymbol{\Theta}_i C_p V_i) &= \mathbf{f}_{\text{ext}} \\ \boldsymbol{\Theta}_i^{\intercal}\mathbf{x} - (C_p)^{-1} q_i = V_i, & \forall i \in [\![1, N]\!] \end{cases} \tag{27}$$

The voltage applied to the electrodes of the ith PZT is $V_i = Z_i Q_i$ in the Laplace domain. Substituting this equation in the second line of (27) gives

$$V_i = \frac{C_p Z_i}{1 + C_p Z_i} \boldsymbol{\Theta}_i^{\intercal} \mathbf{X}. \tag{28}$$

Further, substituting this latter equation in the first line of (27) gives the equations that the impedance Z_i must satisfy to obtain the ABH effect

$$\begin{array}{rcl} \left(2C_p\theta_\phi\right)^2 \dfrac{Z_N}{1+C_pZ_N}\Delta\phi_N & = & -Z_{\mathrm{ABH},\phi}\phi_N^p \\ \dfrac{Z_{i+1}}{1+C_pZ_{i+1}}\Delta\phi_{i+1} & = & \dfrac{Z_i}{1+C_pZ_i}\Delta\phi_i \quad \forall i \in [\![1,N-1]\!]. \end{array} \tag{29}$$

The first equation states that the moment applied by the PZT at the tip must be equal to the moment of the ABH effect (see Equation (3b)). The second equation indicates that adjacent PZTs must produce an equal moment. As a result, the moments will cancel out each other, except at the boundaries. The moment at the clamping does not impact the system's dynamics whereas the moment at the tip mimicks the ABH effect. Equations (29) can be recast into

$$\begin{array}{rcl} Z_N & = & \dfrac{1}{C_p}\left(\dfrac{4C_p\theta_\phi^2\Delta\phi_N}{4C_p\theta_\phi^2\Delta\phi_N + Z_{\mathrm{ABH},\phi}\phi_N} - 1\right) \\ Z_i & = & \dfrac{1}{C_p}\left(\dfrac{\Delta\phi_i\left(1+C_pZ_{i+1}\right)}{\Delta\phi_i\left(1+C_pZ_{i+1}\right) - C_pZ_{i+1}\Delta\phi_{i+1}} - 1\right) \quad \forall i \in [\![1,N-1]\!]. \end{array} \tag{30}$$

which enables to compute the impedance for the different PZTs to reproduce the ABH effect.

A simplification of this approach is to consider the PZTs connected in parallel. They are thus all subjected to the same voltage whereas their charges add up. Summing the electrical equations for $i = 1,\cdots,N$, Equations (27) become

$$\left\{\begin{array}{rcl} \mathbf{M}\ddot{\mathbf{x}} + \mathbf{C}\dot{\mathbf{x}} + \mathbf{K}_{\mathrm{sc}}\mathbf{x} + 2V\theta_\phi\phi_N^pC_p & = & \mathbf{f}_{\mathrm{ext}} \\ 2\theta_\phi\phi_N - \left(C_p\right)^{-1}\displaystyle\sum_{i=1}^{N} Q_i = NV & & \end{array}\right. \tag{31}$$

The moments of adjacent PZTs directly cancel out each other, and only the equality condition between the moment at beam tip and that of the ABH must be enforced. In this case, a single control law is defined

$$V = \mathbf{Z}\sum_{i=1}^{N} Q_i. \tag{32}$$

with

$$Z = \frac{1}{NC_p}\left(\frac{\left(2C_p\theta_\phi\right)^2}{\left(2C_p\theta_\phi\right)^2 + NC_pZ_{\mathrm{ABH},\phi}} - 1\right). \tag{33}$$

References

[1] H. Frahm, Device for damping vibrations of bodies (Apr. 1911).
URL https://patents.google.com/patent/US989958A/en

[2] O. J., D. H. J., Theory of the dynamic vibration absorber, Journal of Applied Mechanics 50 (7) (1928) 11–22.

[3] M. Mironov, Propagation of a flexural wave in a plate whose thickness decreases smoothly to zero in a finite interval, Sov. Phys. Acoust. 34 (1988) 318–319.

[4] V. V. Krylov, F. J. B. S. Tilman, Acoustic 'black holes' for flexural waves as effective vibration dampers, Journal of Sound and Vibration 274 (3) (2004) 605–619. doi:10.1016/j.jsv.2003.05.010.

[5] S. C. Conlon, J. B. Fahnline, F. Semperlotti, Numerical analysis of the vibroacoustic properties of plates with embedded grids of acoustic black holes, The Journal of the Acoustical Society of America 137 (1) (2015) 447, publisher: Acoustical Society of AmericaASA. doi:10.1121/1.4904501.

[6] O. Aklouche, A. Pelat, S. Maugeais, F. Gautier, Scattering of flexural waves by a pit of quadratic profile inserted in an infinite thin plate, Journal of Sound and Vibration 375 (2016) 38–52. doi:10.1016/j.jsv.2016.04.034.

[7] J. Y. Lee, W. Jeon, Vibration damping using a spiral acoustic black hole, The Journal of the Acoustical Society of America 141 (3) (2017) 1437–1445, publisher: Acoustical Society of America. doi:10.1121/1.4976687.

[8] T. Zhou, L. Cheng, A resonant beam damper tailored with Acoustic Black Hole features for broadband vibration reduction, Journal of Sound and Vibration 430 (2018) 174–184. doi:10.1016/j.jsv.2018.05.047.

[9] N. W. Hagood, A. von Flotow, Damping of structural vibrations with piezoelectric materials and passive electrical networks, Journal of Sound and Vibration 146 (2) (1991) 243–268. doi:10.1016/0022-460X(91)90762-9.

[10] H. Yu, K. W. Wang, Piezoelectric Networks for Vibration Suppression of Mistuned Bladed Disks, Journal of Vibration and Acoustics 129 (5) (2007) 559–566. doi:10.1115/1.2775511.

[11] D. Alaluf, B. Mokrani, K. Wang, A. Preumont, Damping of piezoelectric space instruments: application to an active optics deformable mirror, CEAS Space Journal 11 (4) (2019) 543–551. doi:10.1007/s12567-019-00278-4.

[12] L. Zhang, G. Kerschen, L. Cheng, Electromechanical Coupling and Energy Conversion in a PZT-Coated Acoustic Black Hole Beam, International Journal of Applied Mechanics 12 (08) (2020) 2050095, publisher: World Scientific Publishing Co. doi:10.1142/S1758825120500957.

[13] H. Li, C. Touzé, A. Pelat, F. Gautier, Combining nonlinear vibration absorbers and the Acoustic Black Hole for passive broadband flexural vibration mitigation, International Journal of Non-Linear Mechanics 129 (2021) 103558. doi:10.1016/j.ijnonlinmec.2020.103558.

[14] Y. Zhen, H. Li, Y. Tang, Novel vibration control method of acoustic black hole plates using active–passive piezoelectric networks, Thin-Walled Structures 186 (2023) 110705. doi:10.1016/j.tws.2023.110705.

[15] A. J. Fleming, S. Behrens, S. O. R. Moheimani, Synthetic impedance for implementation of piezoelectric shunt-damping circuits, Electronics Letters 36 (18) (2000) 1525–1526, publisher: IET Digital Library. doi:10.1049/el:20001083.

[16] G. Matten, M. Collet, S. Cogan, E. Sadoulet-Reboul, Synthetic Impedance for Adaptive Piezoelectric Metacomposite, Procedia Technology 15 (2014) 84–89. doi:10.1016/j.protcy.2014.09.037.

[17] C. Sugino, M. Ruzzene, A. Erturk, Design and Analysis of Piezoelectric Metamaterial Beams With Synthetic Impedance Shunt Circuits, IEEE/ASME Transactions on Mechatronics 23 (5) (2018) 2144–2155, conference Name: IEEE/ASME Transactions on Mechatronics. doi:10.1109/TMECH.2018.2863257.

[18] K. Yi, G. Matten, M. Ouisse, E. Sadoulet-Reboul, M. Collet, G. Chevallier, Programmable metamaterials with digital synthetic impedance circuits for vibration control, Smart Materials and Structures 29 (3) (2020) 035005, publisher: IOP Publishing. doi:10.1088/1361-665X/ab6693.

[19] G. Raze, A. Jadoul, S. Guichaux, V. Broun, G. Kerschen, A digital nonlinear piezoelectric tuned vibration absorber, Smart Materials and Structures 29 (1) (2019) 015007, publisher: IOP Publishing. doi:10.1088/1361-665X/ab5176.

[20] M. Alshaqaq, C. Sugino, A. Erturk, Programmable Rainbow Trapping and Band-Gap Enhancement via Spatial Group-Velocity Tailoring in Elastic Metamaterials, Physical Review Applied 17 (2) (2022) L021003, publisher: American Physical Society. doi:10.1103/PhysRevApplied.17.L021003.

[21] F. Maugan, S. Chesne, M. Monteil, M. Collet, K. Yi, Enhancement of energy harvesting using acoustical-black-hole-inspired wave traps, Smart Materials and Structures 28 (7) (2019) 075015, publisher: IOP Publishing. doi:10.1088/1361-665X/ab1f11.

[22] C. Sugino, M. Alshaqaq, A. Erturk, Spatially programmable wave compression and signal enhancement in a piezoelectric metamaterial waveguide, Physical Review B 106 (17) (2022) 174304, publisher: American Physical Society. doi:10.1103/PhysRevB.106.174304.

[23] S. Soleimanian, G. Petrone, F. Franco, S. De Rosa, P. Kołakowski, Numerical realization of a semi-active virtual acoustic black hole effect, Frontiers in Mechanical Engineering 9 (2023).

[24] S. Quaegebeur, G. Raze, L. Cheng, G. Kerschen, A virtual acoustic black hole on a cantilever beam, Journal of Sound and Vibration 554 (2023) 117697. doi:10.1016/j.jsv.2023.117697.

[25] O. Thomas, J.-F. Deü, J. Ducarne, Vibrations of an elastic structure with shunted piezoelectric patches: efficient finite element formulation and electromechanical coupling coefficients, International Journal for Numerical Methods in Engineering 80 (2) (2009) 235–268. doi:10.1002/nme.2632.

[26] S. Y. Yang, W. H. Huang, Is a collocated piezoelectric sensor/actuator pair feasible for an intelligent beam?, Journal of Sound and Vibration 216 (3) (1998) 529–538. doi:10.1006/jsvi.1998.1753.

[27] Y.-S. Lee, Comparison of collocation strategies of sensor and actuator for vibration control, Journal of Mechanical Science and Technology 25 (1) (2011) 61–68. doi:10.1007/s12206-010-1102-0.

[28] A. Preumont, Collocated versus Non-collocated Control, in: A. Preumont (Ed.), Vibration Control of Active Structures: An Introduction Third Edition, Solid Mechanics and Its Applications, Springer Netherlands, Dordrecht, 2011, pp. 117–130. doi:10.1007/978-94-007-2033-6_6.

[29] A. Lazarus, O. Thomas, J. F. Deü, Finite element reduced order models for nonlinear vibrations of piezoelectric layered beams with applications to NEMS, Finite Elements in Analysis and Design 49 (1) (2012) 35–51. doi:10.1016/j.finel.2011.08.019.

[30] R. Craig, M. Bampton, Coupling of substructures for dynamic analyses., AIAA Journal 6 (7) (1968) 1313–1319. doi:10.2514/3.4741.

[31] A. Preumont, Stability, in: A. Preumont (Ed.), Vibration Control of Active Structures: An Introduction Third Edition, Solid Mechanics and Its Applications, Springer Netherlands, Dordrecht, 2011, pp. 299–316. doi:10.1007/978-94-007-2033-6_13.